Journal of Materials Chemistry A

Materials for energy and sustainability

Accepted Manuscript

Journal of Materials Chemistry A

Materials for energy and sustainability

rsc.li/materials-a

Volume 6
Number 12
28 March 2018
Pages 4883-5230

ISSN 2050-7488

ROYAL SOCIETY OF CHEMISTRY

COMMUNICATION
Zhenhai Wen et al
An electrochemically neutralized energy-assisted low-cost acid-alkaline electrolyzer for energy-saving electrolysis hydrogen generation

ROYAL SOCIETY OF CHEMISTRY

rsc.li/materials-a

Journal Name

ARTICLE

Highly Efficient Catalysts for Oxygen Reduction using Well-dispersed Iron Carbide Nanoparticles Embedded in the Multichannel Hollow Nanofibers

Hongyin Xia[ab], Shan Zhang[a], Xiaoqing Zhu[a], Huanhuan Xing[a], Yuan Xue[ab], Bolong Huang[c]*, Mingzi Sun[c], Jing Li[a]*, and Erkang Wang[a]*

Engineering the catalytic material into appropriate structures to get the structural benefits is vital for harvesting the unprecedented catalytic efficiency in oxygen reduction reaction (ORR). Herein, well-dispersed and highly active iron carbide nanoparticles (Fe_3C NPs) were encapsulated in multichannel hollow nanofibers (MHNFs) to construct Fe_3C@MHNFs catalysts, which were synthesized via simple electrospinning and calcination steps. The well-defined inner channels with high conductivity and porous structure enable the rapid electron transfer and mass transport for ORR. And the resulting hybrid electrocatalyst with Fe_3C served as active sites exhibits highly efficient activity with a half-wave potential of 0.90 V *vs.* reversible hydrogen electrode (RHE), surpassing that of commercial platinum on carbon (Pt/C) catalyst (the half-wave potential of 0.84 V *vs.* RHE). The catalyst shows robust durability with negligible activity decay after 10,000 cycles. Density functional theory calculations confirm the introduction of MHNFs significantly improves the electron transfer and exchange capability. The formed interfacial region not only induces the linear correlation in both electronic structures and binding energies but also alleviates the barrier of site-to-site electron transfer between Fe_3C NPs and MHNFs for ORR process.

1. Introduction

Increasing energy demands and environmental pollution along with the exhaustion of fossil fuels have promoted extensive efforts in developing clean and sustainable energy resources with a high energy density.[1-3] Thanks to the high energy yield and unlimited source of reactants, fuel cells are expected to be the promising energy conversion systems.[4, 5] As the pivotal half-reaction, the sluggish kinetics of oxygen reduction reaction (ORR) due to the multistep electron transfer pathways determines the overall performance and impedes its commercial application.[6, 7] Platinum

(Pt) electrocatalyst has been regarded as the benchmark for ORR. Unfortunately, it suffers from the limited supply in natural scarcity, high cost and unsatisfactory stability.[8, 9]

To avoid usage of Pt-based catalyst, a variety of nonprecious metal catalysts (NPMCs) with desirable performance have been designed in recent years, including heteroatom-doped carbon materials,[10, 11] transition metal-nitrogen-carbon catalysts,[12] single-atom catalysts,[13] and graphene/transition metal chalcogenides/oxides.[14-16] Composting NPMCs with carbonaceous matrix overcomes the intrinsic weakness of relatively lower electronic conductivity and permits the fast electron transfer to boost the ORR activity. In our previous work, highly active Co_3S_4 nanoparticles (NPs) were in-situ grown on the conductive sulfur-doped graphene matrix for ORR and manifested the matrix-dependent ORR performance.[17] Hou et al. designed the nitrogen-doped core-shell structured porous Fe/Fe_3C@C

[a.] State Key Laboratory of Electroanalytical Chemistry, Changchun Institute of Applied Chemistry, Chinese Academy of Sciences, 5625 Renmin Street, Changchun, Jilin 130022, China. E-mail: ekwang@ciac.ac.cn, lijingce@ciac.ac.cn
[b.] University of Science and Technology of China, Hefei, Anhui, 230026, China.
[c.] Department of Applied Biology and Chemical Technology, The Hong Kong Polytechnic University, Hung Hom, Kowloon, Hong Kong SAR, China. E-mail: bhuang@polyu.edu.hk
† Electronic Supplementary Information (ESI) available. See DOI: 10.1039/x0xx00000x.

ARTICLE

nanoboxes assembled on the reduced graphene oxide sheets with superior electrocatalytic activity.[18] Moreover, optimizing the structural design of the catalytic material or supported substrates with large surface area to get the desirable advantageous also plays a dominant role in obtaining highly catalytic efficiency in ORR. For example, Yang et al. utilized P123 as the template to construct bamboo-like carbon nanotube with high surface area to anchor Fe_3C NPs for highly efficient ORR and demonstrated the morphology-related performance.[19] Currently, benefiting from the rich exposed active sites on hollow and porous structured-carbon matrix for rapid mass transfer, much effort has been made to integrate highly active transition metal-based electrocatalysts on hollow textural matrix for enhancing the overall catalytic activity from two distinct fronts.[20, 21] Meanwhile, the formed interface between active sits and loading matrix provides an ideal strategy to get the benefit of different components at the interface to boost the ORR activity.
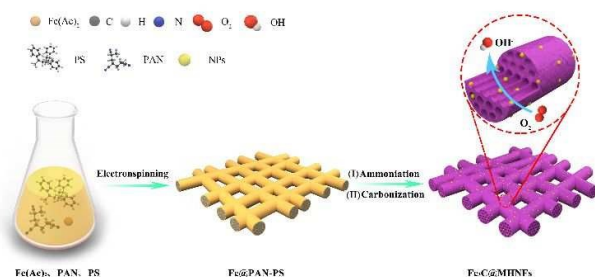
Scheme 1. Schematic illustration of the synthetic process for $Fe_3C@MHNFs$.

Herein, we design a facile protocol to confine Fe_3C NPs in highly conductive multichannel hollow nanofibers (MHNFs) by annealing the uniform Fe@PAN-PS nanofibers, which are obtained through electrospinning method with polystyrene (PS), polyacrylonitrile (PAN) and iron acetate ($Fe(Ac)_2$) as the precursors (Scheme 1). Pyrolysis of the Fe@PAN-PS nanofibers results in the decomposition of the PS, leading to the generation of porous structure, while the metal precursor in the fibers is converted to Fe_3C NPs. Such unique hollow structure of carbon matrix combined with the highly active Fe_3C NPs endows the hybrid improved catalytic activity for ORR. The half-wave potential of $Fe_3C@MHNFs$ for ORR reaches 0.90 V *vs.* reversible hydrogen electrode (RHE) in 0.1 M KOH, which is much more positive than that of commercial Pt/C (half-wave potential of 0.84 V *vs.* RHE).

Moreover, the $Fe_3C@MHNFs$ also exhibits excellent stability and methanol tolerance. Through density functional theory (DFT) calculations, the $Fe_3C@MHNFs$ demonstrates the much-enhanced electron transfer efficiency due to the formation of the highly electroactive interfacial region, which optimizes the electronic environment to facilitate the binding and transformation of the intermediates.

2. Experimental section

2.1 Materials and reagents

PAN (M_W = 150,000), PS, $Fe(Ac)_2$ and Nafion (5 wt. %) were all obtained from Sigma-Aldrich. N, N-dimethylformamide (DMF), methanol and KOH were obtained from Beijing Chemical Reagent Beijing China). Platinum catalyst (20 wt. % Pt/C) was purchased from Alfa Aesar. All chemicals and reagents were used without further purification. All aqueous solutions in this experiment were prepared using deionized water purified by Millipore system.

2.2 Characterization

Scanning electron microscopy (SEM) was carried out on a PHILIPS XL-30 ESEM with an acceleration voltage of 20 kV. Transmission electron microscopy (TEM), high-resolution TEM (HRTEM), high angle annular dark field-scanning transmission electron microscopy (HAADF-STEM) and elemental mapping images were obtained by using a TECNAI G2 (accelerating voltage, 200 kV). Powder X-ray diffraction (XRD) was performed on a Riga-kuD/MAX wide angle X-ray diffractometer with Cu Kα radiation with a λ of 1.5406 Å. X-ray photoelectron spectra (XPS) was carried out on an ESCALAB-MKII X-ray photoelectron spectrometer with Al Kα radiation. Nitrogen sorption isotherms were performed on an ASAP 2020 Physisorption Analyzer. Raman spectra were collected on a Renishaw 2000 model confocal microscopy Raman spectrometer with a CCD detector and a holographic notch filter.

2.3 Preparation of catalysts

Fe@PAN-PS nanofibers: the Fe@PAN-PS nanofibers were prepared according to the previous method with some modification.[20] Specifically, 500 mg PAN, 250 mg PS and 2 mmol $Fe(Ac)_2$ were first dissolved in 5 mL DMF with vigorous stirring for 12 h to obtain the electrospinning precursors. Then the precursor was electrospun by filling into a 5mL syringe with a 19# needle. The

Journal Name ARTICLE

rotating speed of aluminum foil collector was 10 rpm and the applied voltage was set at 20 kV. The electrospinning speed was 0.3 mm min^{-1} and the distance between the needle and the collector was 20 cm. The obtained electrospun samples were denoted as Fe@PAN-PS nanofibers. Finally, the Fe@PAN-PS nanofibers were treated at 200 °C for 6 h in a drying oven.

Fe$_3$C@MHNFs: The above brown Fe@PAN-PS nanofibers were firstly annealed at 500 °C for 2 h at a heating rate of 5 °C min^{-1} in NH$_3$ atmosphere. Afterwards, the product was further annealed up to 900 °C for 2 h with a heating rate of 5 °C min^{-1} under N$_2$ flow. Finally, the black samples of Fe$_3$C@MHNFs were grinded into powder for the preparation of catalyst ink. For comparision, the nanofibers without the participation of PS and Fe(Ac)$_2$ were prepared under the same conditions and labeled as Fe$_3$C@SNFs and MHNFs, respectively. In addition, Fe$_3$C-1@MHNFs and Fe$_3$C-3@MHNFs were prepared by introducing 1 mmol Fe(Ac)$_2$ and 3 mmol Fe(Ac)$_2$ precursor under identical condition as that of Fe$_3$C@MHNFs

2.4 Electrochemical measurements

Catalytic ink preparation: 4 mg powder was dispersed in a mixture of 990 μL ethanol and 10 μL Nafion (5 wt. %) by sonication for at least 60 min. Electrochemical measurements were performed on a CHI 832C electrochemical workstation with a rotation control device based a conventional three-electrode system consisting of a glassy carbon electrode (GCE) as the working electrode, a Hg/HgO electrode as the reference electrode, and a platinum foil as the counter electrode, respectively. 10 μL catalyst ink was dropped on the GCE with a surface area of 0.196 cm^2 to give a loading of 0.20 mg cm^{-2}. Cyclic voltammetry (CV) tests were performed at a scan rate of 20 mV s^{-1} in 0.1 M KOH solution with saturated N$_2$ or O$_2$. Linear sweep voltammetry (LSV) curves were obtained using a rotating disk electrode (RDE) by varying speed rates from 400 to 1600 rpm with a scan rate of 20 mV s^{-1}. Rotating ring-disk electrode (RRDE) voltammetry was carried out with a Pt ring electrode. 12.6 μL catalyst ink was dropped on the RRDE with a surface area of 0.247 cm^2 to give a loading of 0.20 mg cm^{-2} and the ring potential was set at 1.3 V *vs.* RHE. The durability test of the electrocatalysts was conducted by cycling from 0.6 to 1.0 V *vs.* RHE at 50 mV s^{-1} for 10,000 cycles. All control samples were drop-casted onto the electrode with the same loading. All potentials

reported were calibrated to the RHE based on the equation E (RHE) = E (Hg/HgO) + 0.879 V. The calibration was carried out via a hydrogen evolution/oxidation reaction polarization curve of Pt wire (Fig. S1).

2.5 Calculation Setup

We had applied the density functional theory (DFT) within CASTEP packages for the geometry optimization to the Fe$_3$C@MHNFs lattice structure regarding both electronic structures and the energetic reaction trend.[22] For all relaxation, the generalized gradient approximation (GGA) with Perdew-Burke-Ernzerhof (PBE) functionals were selected to describe the electronic exchange-correlation interaction.[23] The plane-wave cutoff energy of 380 eV with the ultrasoft pseudopotentials quality was used in all ground-state relaxations. Meanwhile, the Broyden-Fletcher-Goldfarb-Shannon (BFGS) algorithm was utilized.[24, 25] The Monkhost-Pack reciprocal space integration was performed under coarse quality as a self-consistent approach for total energy minimization.[26] The tolerance settings were as following: ionic force lower than 0.1 eV/Å with total energy lower than 5.0 × 10^{-5} eV/atom; maximum displacement and stress on atom lower than 0.005 Å and 0.2 GPa, respectively. The Fe$_3$C structure consists of 4 layers of the (211) surfaces in a 1×2×1 supercell to combine with MHNFs layers. The MHNFs layer was constructed based on graphene structure with the introduction of pyridinic, graphitic N atoms as the XPS results. The Fe$_3$C@MHNFs lattice included 185 atoms in total with the vacuum space of 20 Å in the z-direction for the all DFT calculations.

3. Results and discussion

3.1 Characterization of the catalysts

The detailed synthetic process of the Fe$_3$C@MHNFs is illustrated in Scheme 1. Briefly, the homogenous mixture of PS, PAN and Fe(Ac)$_2$ was prepared in DMF to fabricate the Fe@PAN-PS nanofibers via electrospinning method. Nitrogen was successfully introduced into the fiber by calcining the Fe@PAN-PS nanofibers under NH$_3$ atmosphere at 500 °C. The subsequent pyrolysis process was conducted at 900 °C in N$_2$ atmosphere to finally prepare the target hybrid of Fe$_3$C@MHNFs.

The SEM image of Fe@PAN-PS nanofibers demonstrated the formation of highly uniform interconnected structure with an

ARTICLE

average diameter of about 500 nm (Fig. 1a). After two-step annealing treatment, the target $Fe_3C@MHNFs$ retained the interwoven fibrous network without obvious changes on the surface (Fig. 1b). However, the cross-sectional morphology displayed lotus root-like structure, signifying the formation of hollow multichannels owing to the partial deposition of PS (Fig. 1c). Meanwhile, the carbonization of PAN and the pyrolytic transformation of $Fe(Ac)_2$ at high temperature led to the homogenously grown of Fe_3C NPs on the conductive multiple channel carbon matrix in either multichannel interiors or on the surface of the fibers (Fig. 1d). The HRTEM image of $Fe_3C@MHNFs$ clearly showed that the Fe_3C NPs were encapsulated by graphite carbon (Fig. 1e). The lattice distance of 0.34 nm and 0.21 nm agreed well with the (300) facet of graphitic carbon and (211) crystal plane of Fe_3C, respectively (Fig. 1f). The C, N and Fe elements coexist and distribute uniformly in the $Fe_3C@MHNFs$ (Fig. 1g), further confirming the formation of Fe_3C NPs throughout the entire matrix.
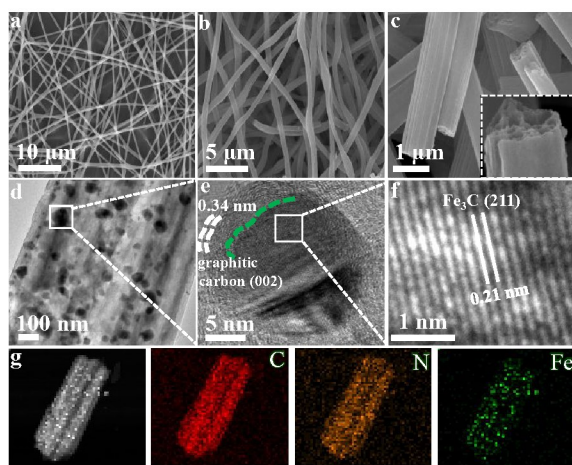

Fig. 1 (a) SEM of Fe@PAN-PS nanofibers; (b and c) SEM, (d) TEM, (e and f) HRTEM, (g) HAADF-STEM and elemental mapping images of $Fe_3C@MHNFs$.

In addition, XRD data of $Fe_3C@MHNFs$ in Fig. 2a showed that the diffraction peak located at 26° is ascribed to the (300) of graphite phase (JCPDS 50-0927). While the diffraction peaks located at 38°, 43°, 44°, 46°, 49° are well assigned to that of the Fe_3C (JCPDS 35-0772). Specifically, the diffraction peak at 43° can be indexed to the (211) plane of Fe_3C. Taking the HRTEM result of $Fe_3C@MHNFs$ into account, the lattice distance of 0.21 nm in Figure 1f, well matched with the d-spacing of (211)

crystallographic plane of Fe_3C. All the above results indicate the successful decoration of Fe_3C on the graphitic carbon.

To investigate the degree of graphitization, the Raman spectrum was conducted (Fig. 2b). Two strong characteristic peaks of carbon at about 1363 cm^{-1} (D-band) and 1603 cm^{-1} (G-band) provide information about the disorder and crystallinity of sp^2 carbon materials. The $Fe_3C@MHNFs$ with the low I_D/I_G ratio of 0.86 indicates more perfect carbon structure and higher degree of graphitization, which will be in favor of improving the electronic conductivity, and thus benefiting higher catalytic performance.[27]
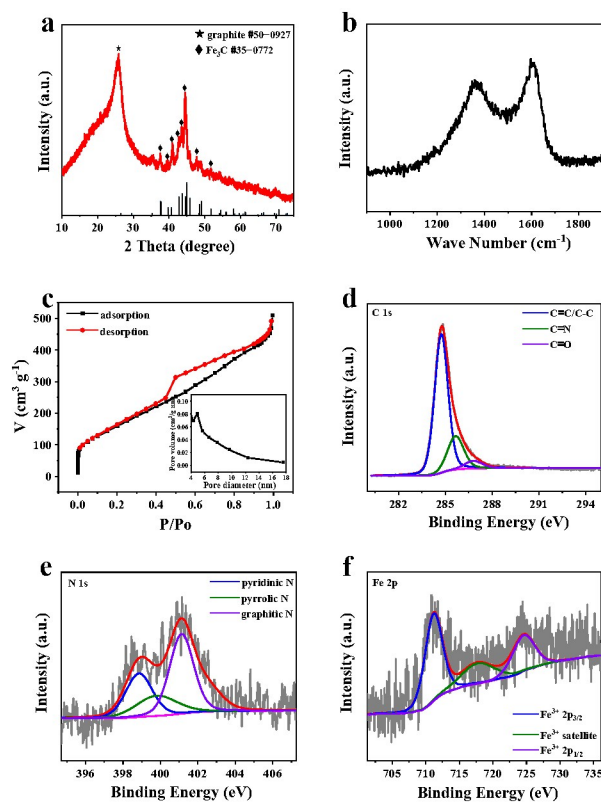

Fig. 2 (a) XRD, (b) Raman, (c) N_2 adsorption-desorption isotherm (the inset shows the pore distribution curve), (d) C 1s XPS spectrum, (e) N 1s XPS spectrum, (f) Fe 2p XPS spectrum of the $Fe_3C@MHNFs$.

The N_2 adsorption and desorption isotherm curves of the as-made $Fe_3C@MHNFs$ showed a large Brunauer-Emmett-Teller (BET) surface area of 607.90 m^2 g^{-1}, and the Barrett-Joyner-Halenda (BJH) analysis indicated the presence of 4.88 nm mesopores (Fig. 2c). For comparison, the $Fe_3C@SNFs$ sample with a shrunken size and closed fiber structure (Fig. S2) showed an obvious decrease of

Journal Name ARTICLE

surface area (279.59 m^2 g^{-1}) (Fig. S3), indicating that the introduction of PS can regulate the morphology and structure of the fibrous matrix to form multichannel hollow structure.

The XPS was further carried out to investigate the chemical composition and valence states of the targeted Fe$_3$C@MHNFs. The Fe$_3$C@MHNFs is mainly composed of C (92.71 at. %), N (2.60 at. %), O (4.24 at. %), and Fe (0.45 at. %) (Fig. S4). The high-resolution C 1s XPS spectrum of the Fe$_3$C@MHNFs (Fig. 2d) can be fitted into three peaks at 284.74, 285.65, and 286.80 eV, corresponding to the C=C/C-C, C=N, and C=O bonds, respectively. It confirms that N had been successfully doped into the carbon structure.[28] The N 1s XPS spectrum of Fe$_3$C@MHNFs is fitted into three nitrogen peaks with the binding energies of 398.85, 399.80 and 401.13 eV, which can be attributed to the pyridinic N, pyrrolic N and graphitic N, respectively.[18] As is shown in Fig. 2e, the Fe$_3$C@MHNFs possesses a high content of pyridinic N. It is widely perceived as the species for increasing the density of π states of the C atoms near the Fermi level to catalyze ORR.[29, 30] In Fe 2p XPS spectrum (Fig. 2f), the peaks at 711.17, 717.73, and 724.55 eV are assigned to Fe^{3+} 2p$_{3/2}$, shake-up satellite Fe^{3+} 2p$_{3/2}$ and Fe^{3+} 2p$_{1/2}$, respectively.[10]

3.2 ORR activity of the catalysts

Encouraged by the high-dispersion Fe$_3$C NPs sites and multichannel hollow structure, the ORR activity of the Fe$_3$C@MHNFs was first evaluated by CV curves at room temperature. As control, the performance of MHNFs and Fe$_3$C@SNFs for ORR was collected. As shown in Fig. 3a, the metal-free MHNF showed poor activity compared with that of Fe$_3$C@MHNFs, manifesting the high activity originates from the Fe$_3$C NPs. And compared with Fe$_3$C@SNFs, the Fe$_3$C@MHNFs showed higher ORR activity, indicating the better capability for O$_2$ absorption of hollow multichannel structure (Fig. S2). The ORR activity of the as-prepared electrocatalysts was then evaluated with the RDE (Fig. 3b). A half-wave potential (E$_{1/2}$) of 0.90 V and the limiting current density (J$_K$) of 5.81 mA cm^{-2} were obtained with Fe$_3$C@MHNFs, which was superior to those of MHNFs (E$_{1/2}$ = 0.69 V, J$_K$ = 2.14 mA cm^{-2}), Fe$_3$C@SNFs (E$_{1/2}$ = 0.79 V, J$_K$ = 3.93 mA cm^{-2}), even better than that of Pt/C (E$_{1/2}$ = 0.84 V, J$_K$ = 5.30 mA cm^{-2}) (Fig. 3c). The superior performance of Fe$_3$C@MHNFs to Fe$_3$C@SNFs and MHNFs clearly indicates that the great advantage obtained by engineering highly active Fe$_3$C sites into unique

MHNFs structure. The hollow matrix can promote mass transfer and improve O$_2$ adsorption. Moreover, the interfacial region between Fe$_3$C sites and hollow carbon matrix significantly boost ORR performance.
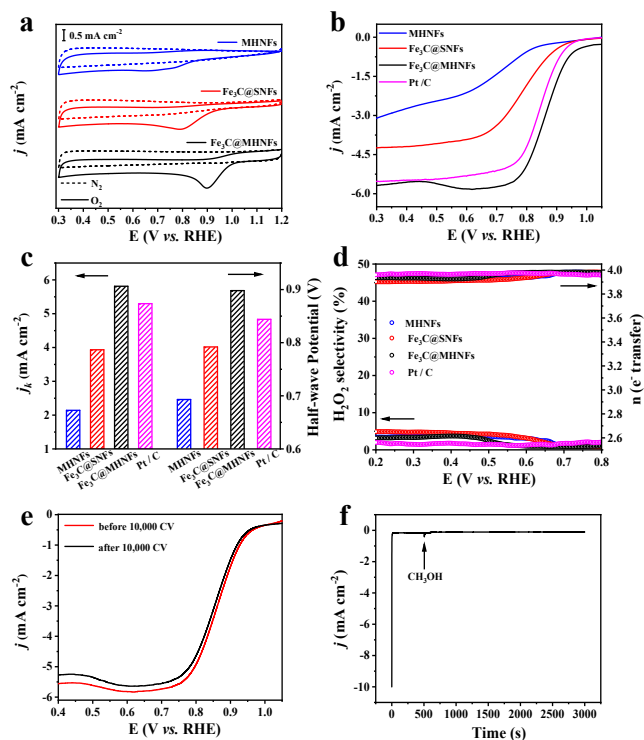

Fig. 3 (a) CV curves of MHNFs, Fe$_3$C@SNFs, and Fe$_3$C@MHNFs in N$_2$ (dotted line) and O$_2$ (solid line) saturated 0.1 M KOH. (b) Polarization curves of MHNFs, Fe$_3$C@SNFs, Fe$_3$C@MHNFs and commercial Pt/C. (c) Limiting current density at 0.60 V *vs.* RHE and E$_{1/2}$ of MHNFs, Fe$_3$C@SNFs, Fe$_3$C@MHNFs and Pt/C. (d) H$_2$O$_2$ % and electron transfer number of MHNFs, Fe$_3$C@SNFs, Fe$_3$C@MHNFs and Pt/C. (e) LSV curves for Fe$_3$C@MHNFs before and after 10,000 cycles. (f) Chronoamperometric curve of Fe$_3$C@MHNFs for methanol crossover test.

Afterwards, ORR polarization curves of the Fe$_3$C@MHNFs at different rotation rates ranging from 400 to 1600 rpm were recorded to investigate the electron transfer mechanism (Fig. S5a). On the basis of the Koutecky-Levich equation, the J^{-1} vs. ω$^{-1/2}$ plots was obtained. The electron transfer number (n) calculated from the slope of each line was about 4 (Fig. S5b). The RRDE measurements further confirmed the efficient four-electron ORR process with a relative low peroxide yield of less than 5 % (Fig. 3d).

ARTICLE

Journal Name

Furthermore, durability experiments were performed to test the stability of Fe₃C@MHNFs (Fig. 3e). The polarization curve recorded after 10,000 cycles indicate its good durability with slight change of limiting current density. Moreover, there was almost no change in current density after the addition of 1.0 M methanol, demonstrating the excellent durability and methanol tolerance (Fig. 3f).

3.3 DFT calculations

DFT calculations were further applied to study the improved ORR performances induced by the introduction of MHNFs to the Fe₃C. The Fe₃C@MHNFs system has displayed strong binding with the MHNFs layers through both C and N sites. The formation of the interface exhibits distortion to the bottom layer of Fe₃C, causing different bonding and non-bonding Fe sites in the interfacial region (Fig. 4a). The 3D contour plot of the electronic distribution clearly reveals the contribution of the MHNFs substrate to the anti-bonding and bonding orbitals near the Fermi level (E$_F$), which supports the enhanced electron density for promoting the ORR (Fig. 4b). The projected partial density of states (PDOS) demonstrates the electroactivity of Fe₃C@MHNFs locates on the Fe sites, which display a small e$_g$-t$_{2g}$ splitting gap to accomplish the electron transfer towards the adsorbates. The C-s,p orbitals show the electron-rich structure, which efficiently supplies the electrons for reduction. Notably, the s,p orbitals of MHNFs demonstrate the broadband feature, accompanying with the crossing of E$_F$, supporting an enhancement to the electron conductivity to the Fe₃C. With the introduction of π-electron-rich MHNFs, the site-to-site electrons transfer for ORR has been significantly boosted (Fig. 4c). Within the Fe₃C@MHNFs, the e$_g$-t$_{2g}$ splitting gap remained almost unchanged from the surface to the interfacial region near MHNFs. However, the upshifting of Fe-t$_{2g}$ leads to the higher energy barrier of electron transfer from C sites. It is noted that the interfacial Fe sites have shown two different electronic structures depending on the bonding (IF-Fe-B) and non-bonding (IF-Fe-NB) with MHNFs. The bonding Fe sites display a similar electroactivity with the surface Fe, confirming the activation of the Fe₃C by the MHNFs substrate (Fig. 4d). Such an influence is also noted in C sites within Fe₃C, where both surface C and interfacial C sites demonstrate much closer positions to the E$_F$. This indicates the obvious alleviation of the barrier of site-to-site

electron transfer between Fe and C sites. Meanwhile, different C sites in MHNFs both reveal the electron density near E$_F$, further support the good conductivity of MHNFs (Fig. 4e). In addition, the electronic structures of key intermediates are illustrated. For all the O-related species, the clear linear correlation of the dominant peak of s,p orbitals along the reaction coordinates guarantees the efficient electron transfer from the initial O₂ adsorption to the final reduction in the alkaline environment (Fig. 4f).
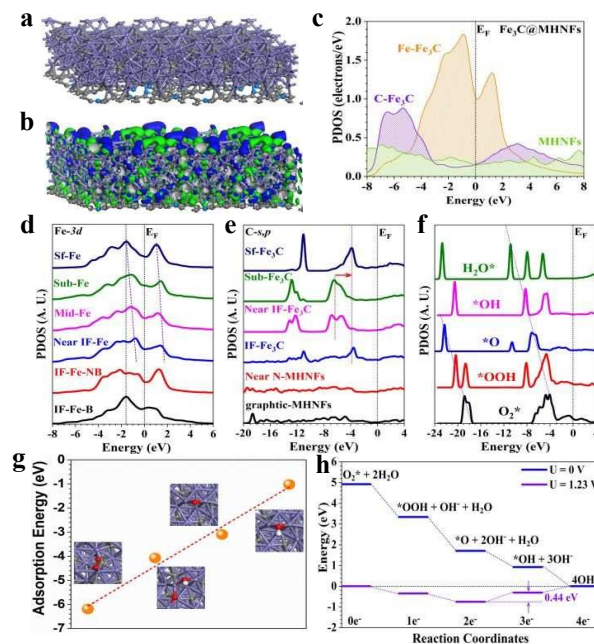

Fig. 4 (a) The structure of Fe₃C@MHNFs. (b) The 3D contour plot of the bonding and anti-bonding orbitals near E$_F$ in Fe₃C@MHNFs. (c) The PDOSs of Fe₃C@MHNFs. (d) The site-dependent PDOSs of Fe-3d orbitals in Fe₃C@MHNFs. (e) The site-dependent PDOSs of C-s,p orbitals in Fe₃C@MHNFs. (f) The PDOSs of intermediates binding on the Fe₃C@MHNFs during ORR. (g) The PDOSs of Fe₃C@MHNFs. (h) The energetic pathway of ORR on Fe₃C@MHNFs.

From the electronic environment optimized by the introduction of MHNFs, the binding energies also reflect the linear relationship of the intermediates in the most stable structural configurations. The initial binding of O₂ is very strong with a binding energy of -6.20 eV, laying a good foundation for the subsequent reduction process. More importantly, we notice the dissociation of *OOH after relaxation, supporting a spontaneous trend for the transformation from [*OOH] to [*OH]. As the electrons have been

Journal Name ARTICLE

transferred to the intermediates, the binding of the intermediates also becomes weaker, which guarantees the efficient desorption of *OH for the ORR process. These results confirm the linear correlation from both electronic and energetic perspectives along the reaction pathway (Fig. 4g).   For the reaction pathway of ORR, the overall process delivers the exothermic trend at the equilibrium state with U = 0 V. The transformation of [*O$_2$] to [*OOH] and [*OOH] to [*O] exhibit the energy drop of 1.58 and 1.63 eV, respectively, supporting the spontaneous trend. This is also consistent with the strong binding energies of intermediates. With the applied potential of U = 1.23 V, the hydrogenation of [*O] demonstrates the only energy barrier of 0.44 eV, which reveals that the overpotential of the ORR performance on Fe$_3$C@MHNFs is close to experimental results (Fig. 4h). Therefore, the significantly improved ORR process on Fe$_3$C@MHNFs is attributed to the improved electron transfer capability due to the optimization of the electronic environment induced by the strong interaction between Fe$_3$C and MHNFs.

Furthermore, a series of control experiments were conducted to better clarify the outstanding ORR activity from the Fe$_3$C@MHNFs. To highlight the significance of well-dispersed Fe$_3$C NPs, Fe$_3$C-1@MHNFs and Fe$_3$C-3@MHNFs were prepared as control. As shown in Fig. S6, more Fe$_3$C NPs were loaded on the hollow multichannel matrix with the increase of Fe(Ac)$_2$, and the improved ORR activity was observed due to the increased active sites. However, when the concentration of Fe(Ac)$_2$ was up to 3 mmol, the electrocatalytic activity obviously decreased (Fig. S7), which may be attributed to the aggregation of Fe$_3$C NPs. Additionally, to demonstrate the necessity of NH$_3$ treatment, the eletrocatalysts (named A-Fe$_3$C@MHNFs) prepared with the same procedure of Fe$_3$C@MHNFs except instead of the NH$_3$ using N$_2$ were prepared. Apparently, without the participation of NH$_3$, more negative E$_{1/2}$ and much smaller limiting current density were obtained. It suggested the decrease of pyridinic N led to low-density loading of Fe$_3$C NPs (Fig. S8 and Table S2). Besides, suitable pyrolysis temperature favored to form the high degree of graphitization for improving ORR performance (Fig. S9).

4. Conclusion

In summary, we had presented a simple synthetic strategy for the controlled synthesis of Fe$_3$C@MHNFs by electrospinning and pyrolysis for enhanced ORR. Through controlling the compositions of the precursor, the as-prepared catalysts can be finely tuned in the aspects of morphology, surface area, porosity, and proportion of active sites. Under the optimal conditions, the obtained Fe$_3$C@MHNFs possessed a lager surface area, MHNFs network (matrix), and abundant Fe$_3$C NPs active sites as well as high proportion of graphitic carbon, thus exhibiting outstanding ORR performance, superior to commercial Pt/C. Moreover, Fe$_3$C@MHNFs also showed long-term stability and good methanol tolerance. Due to the MHNFs introduction, DFT calculations revealed the linear correlations along the reduction process in both the electronic properties and the binding energies of the intermediates, which is the key to realize the efficient electron transfer and intermediates transformation of ORR. This work provides offers a new protocol to design porous nanofibers/NPs composites with highly catalytic activity and will help guide the future development of NPMCs in energy conversion technologies.

Conflicts of interest

There are no conflicts of interest to declare.

Acknowledgements

Notes and references

1. L. Tao, Y. Wang, Y. Zou, N. Zhang, Y. Zhang, Y. Wu, Y. Wang, R. Chen and S. Wang, *Adv. Energy Mater.*, 2019, **10,** 1901227.
2. Z. W. Seh, J. Kibsgaard, C. F. Dickens, I. B. Chorkendorff, J. K. Norskov and T. F. Jaramillo, *Science*, 2017, **355,** 4998-5009.
3. Y. Huang, Y. Wang, C. Tang, J. Wang, Q. Zhang, Y. Wang and J. Zhang, *Adv. Mater.,* 2019, **31,** 1803800.
4. D. Higgins, P. Zamani, A. Yu and Z. Chen, *Energy Environ. Sci.,* 2016, **9,** 357-390.
5. J. Shui, C. Chen, L. Grabstanowicz, D. Zhao and D.-J. Liu, *Proc. Natl. Acad. Sci. U. S. A.,* 2015, **112,** 10629-10634.
6. M. Liu, Z. Zhao, X. Duan and Y. Huang, *Adv. Mater.*, 2019, **31,** 1802234.
7. X. X. Wang, M. T. Swihart and G. Wu, *Nat. Catal.,* 2019, **2,** 578-589.
8. X. Tian, X. Zhao, Y.-Q. Su, L. Wang, H. Wang, D. Dang, B. Chi, H. Liu, E. J. M. Hensen, X. W. Lou and B. Y. Xia, *Science,* 2019, **366,** 850-856.

Journal of Materials Chemistry A Accepted Manuscript

ARTICLE

Journal Name

9. Y. Yuan, J. Wang, S. Adimi, H. Shen, T. Thomas, R. Ma, J. P. Attfield and M. Yang, *Nat. Mater.,* 2020, **19,** 282-286.

10. J. Zhang, M. Zhang, Y. Zeng, J. Chen, L. Qiu, H. Zhou, C. Sun, Y. Yu, C. Zhu and Z. Zhu, *Small,* 2019, **15,** 1900307.

11. L. Yang, J. Shui, L. Du, Y. Shao, J. Liu, L. Dai and Z. Hu, *Adv. Mater.,* 2019, **31,** 1804799.

12. S. H. Ahn, X. Yu and A. Manthiram, *Adv. Mater.,* 2017, **29,** 1606534.

13. X. Zhang, S. Zhang, Y. Yang, L. Wang, Z. Mu, H. Zhu, X. Zhu, H. Xing, H. Xia, B. Huang, J. Li, S. Guo and E. Wang, *Adv. Mater.,* 2020, **32,** 1906905.

14. P. Chen, T. Zhou, L. Xing, K. Xu, Y. Tong, H. Xie, L. Zhang, W. Yan, W. Chu, C. Wu and Y. Xie, *Angew. Chem. Int. Ed.,* 2017, **56,** 610-614.

15. H. Shen, E. Gracia-Espino, J. Ma, K. Zang, J. Luo, L. Wang, S. Gao, X. Mamat, G. Hu, T. Wagberg and S. Guo, *Angew. Chem. Int. Ed.,* 2017, **56,** 13800-13804.

16. D. Ji, L. Fan, L. Tao, Y. Sun, M. Li, G. Yang, Q. T. Thang, S. Ramakrishna and S. Guo, *Angew. Chem. Int. Ed.,* 2019, **58,** 13840-13844.

17. W. Gu, L. Hu, W. Hong, X. Jia, J. Li and E. Wang, *Chem. Sci.,* 2016, **7,** 4167-4173.

18. Y. Hou, T. Huang, Z. Wen, S. Mao, S. Cui and J. Chen, *Adv. Energy Mater.,* 2014, **4,** 1400337.

19. W. Yang, X. Liu, X. Yue, J. Jia and S. Guo, *J. Am. Chem. Soc.,* 2015, **137,** 1436-1439.

20. Y. Wang, S. Wang and X. W. Lou, *Angew. Chem. Int. Ed.,* 2019, **58,** 17236-17240.

21. H. Zhang, W. Zhou, T. Chen, B. Y. Guan, Z. Li and X. W. Lou, *Energy Environ. Sci.,* 2018, **11,** 1980-1984.

22. S. J. Clark, M. D. Segall, C. J. Pickard, P. J. Hasnip, M. J. Probert, K. Refson and M. C. Payne, *Z. Kristall.,* 2005, **220,** 567-570.

23. J. P. Perdew, K. Burke and M. Ernzerhof, *Phys. Rev. Lett.,* 1996, **77,** 3865-3868.

24. J. D. Head and M. C. Zerner, *Chem. Phys. Lett.,* 1985, **122,** 264-270.

25. P. J. Hasnip and C. J. Pickard, *Comput. Phys. Commun.,* 2006, **174,** 24-29.

26. M. I. J. Probert and M. C. Payne, *Phys. Rev. B,* 2003, **67,** 11.

27. L. Lin, Q. Zhu and A.-W. Xu, *J. Am. Chem. Soc.,* 2014, **136,** 11027-11033.

28. W. Yang, J. Zhou, S. Wang, W. Zhang, Z. Wang, F. Lv, K. Wang, Q. Sun and S. Guo, *Energy Environ. Sci.,* 2019, **12,** 1605-1612.

29. D. Guo, R. Shibuya, C. Akiba, S. Saji, T. Kondo and J. Nakamura, *Science,* 2016, **351,** 361-365.

30. S. K. Singh, K. Takeyasu and J. Nakamura, *Adv. Mater.,* 2019, **31,** 1804297.

Journal of Materials Chemistry A Accepted Manuscript